

# Variational Deep Image Restoration

Jae Woong Soh, *Student Member, IEEE*, and Nam Ik Cho, *Senior Member, IEEE*

**Abstract**—This paper presents a new variational inference framework for image restoration and a convolutional neural network (CNN) structure that can solve the restoration problems described by the proposed framework. Earlier CNN-based image restoration methods primarily focused on network architecture design or training strategy with non-blind scenarios where the degradation models are known or assumed. For a step closer to real-world applications, CNNs are also blindly trained with the whole dataset, including diverse degradations. However, the conditional distribution of a high-quality image given a diversely degraded one is too complicated to be learned by a single CNN. Therefore, there have also been some methods that provide additional prior information to train a CNN. Unlike previous approaches, we focus more on the objective of restoration based on the Bayesian perspective and how to reformulate the objective. Specifically, our method relaxes the original posterior inference problem to better manageable sub-problems and thus behaves like a divide-and-conquer scheme. As a result, the proposed framework boosts the performance of several restoration problems compared to the previous ones. Specifically, our method delivers state-of-the-art performance on Gaussian denoising, real-world noise reduction, blind image super-resolution, and JPEG compression artifacts reduction.

**Index Terms**—Image Restoration, Variational Approximation, Image Denoising, Image Super-Resolution, JPEG Compression Artifacts Reduction

## I. INTRODUCTION

IMAGE restoration is an important low-level vision problem because the images are usually corrupted by many kinds of degradation during the imaging and transmission processes. It is typically an ill-posed inverse problem because the image degradation procedures are irreversible. Some examples of degradations are noise corruption, blurring, spatial subsampling, compression artifacts, etc., and there have been many approaches to alleviating or restoring from degradations. Image restoration aims to enhance the visual quality of images for human observability and play the role of preprocessing to boost other high-level vision tasks' performances.

The image degradation is generally modeled as

$$\mathbf{y} = T(\mathbf{x}) + \mathbf{n}, \quad (1)$$

where  $\mathbf{y}$ ,  $\mathbf{x}$ , and  $\mathbf{n}$  denote an observed low-quality image, its corresponding high-quality image, and additive noise, respectively.  $T(\cdot)$  represents the degradation function, which is usually non-invertible. The overall goal of the image restoration problem can be regarded as to learn the underlying posterior distribution  $p(\mathbf{x}|\mathbf{y})$ , and many classical methods estimate the

clean image  $\mathbf{x}$  based on the maximum-a-posteriori (MAP) inference, with the appropriately designed priors. Traditionally, handcrafted priors have played an important role in this approach, where appropriate domain-relevant and task-relevant priors were designed for the given kind of restoration problem. In the Bayesian perspective, the MAP inference can be divided into likelihood term and prior term as

$$\hat{\mathbf{x}} = \arg \max_{\mathbf{x}} \log p(\mathbf{x}|\mathbf{y}), \quad (2)$$

$$= \arg \max_{\mathbf{x}} \log p(\mathbf{y}|\mathbf{x}) + \log p(\mathbf{x}). \quad (3)$$

The likelihood term is usually modeled as L2-norm based on the Gaussian noise assumption (task-relevant prior), and the prior term is designed based on experience and knowledge about natural images (domain-relevant prior). Some of widely used priors are total variation, sparsity, low-rankness, and non-local self-similarity [1]–[10]. These strong priors often work well, but explicit constraints on the design limit the performance compared to current data-driven methods.

Recently, CNNs have shown breakthrough performances in overall image restoration problems [11]–[20] by learning the mapping between  $\mathbf{y}$  and  $\mathbf{x}$ , *i.e.*, by implicitly learning the priors. Most of the early works aimed at non-blind image restoration, or in other words, aimed at specific cases where the degradation information such as noise level for denoising or blur kernel for super-resolution is known. Given the specific degradation models, they generally focused on network architecture design, training datasets, and learning strategies. Afterward, some works focused on more practical solutions such that a single network can cope with diverse degradations [12], [21]–[25], or blind scenarios [17], [26]–[29]. Meanwhile, some researchers addressed the problem of the blurry results due to the use of pixel-wise mean squared error (MSE) loss and thus investigated new target objectives based on the generative adversarial net (GAN) [30] [31]–[34].

The above-stated non-blind restoration methods, which we will refer to as “specific models,” are not practical because we need to prepare many separate networks to cope with diverse degradation models. When an input image bears a degradation different from the trained one, a severe performance drop occurs due to the domain discrepancy between training and test image distributions. To alleviate this problem, naïve blind models are proposed, in which a single network is trained with a training dataset consisted of images having various degradations with broad parameter ranges [11], [35]–[37]. However, the naïve blind model generally performs worse than the non-blind one for a given specific degradation because the conditional distribution  $p(\mathbf{x}|\mathbf{y})$  of the blind training dataset is more diverse and difficult to learn than that of the non-blind one.

J. W. Soh and N. I. Cho are with the Department of Electrical and Computer Engineering, Seoul National University, INMC, Seoul, Korea. Corresponding: nicho@snu.ac.kr. This work was supported in part by the National Research Foundation of Korea(NRF) grant funded by the Korea government(MSIT) (2021R1A2C2007220), and in part by Samsung Electronics Co., Ltd.

Manuscript received April 19, 2005; revised August 26, 2015.

Hence, instead of the naïve blind training, some methods adopted the two-stage framework for blind image restoration, which is a combination of estimator and restorer. The estimator extracts features related to task-specific prior information, which is fed to the restorer along with the input image [12], [20], [21], [25], [29], [38]. The restorer is trained to adjust its behavior according to the input and the prior information from the estimator. The prior information in these methods is generally defined based on human knowledge, where the parameters of the degradation are learned by supervised training. For example, they defined the prior knowledge as the spatially varying noise variance map in the case of image denoising. Based on previous approaches and their results, we hypothesize that providing additional information can be interpreted as dividing a complex distribution into simpler sub-distributions. Thus, it will eventually make the network easier to learn the overall task, further boosting the performance.

Meanwhile, earlier methods trained the networks with synthetic datasets that deviate from the real-world situation. For example, the additive white Gaussian noise (AWGN) model is assumed when constructing datasets for denoising, and the synthetic decimation model with the bicubic blur kernel is used for the single image super-resolution (SISR). Since real-world degradations are different from these assumptions, many researchers also developed CNNs to restore the real-world degraded images [38]–[47]. The restoration of real-world images has been a challenging task, mainly in two aspects. First, it is hard to build a paired dataset  $\{\mathbf{y}_i, \mathbf{x}_i\}_{i=1}^N$  for the real-world scenario. Some works assumed degradations with more complex parametric models such as heteroscedastic or Poisson mixture noise [48]–[51]. Some others imitated complex degradation based on camera pipeline [38], [52]–[54]. Instead of model-based methods, several methods learned the degradation based on generative models such as GAN [55], [56] or normalizing flow [57]. Some researchers have taken many pairs of real-world images with careful considerations (misalignment, brightness, clipping, etc.) and precise image acquisition settings [40], [41], [44]–[47]. These methods can alleviate the data scarcity problem, but such acquisition processes are costly and labor-intensive. Second, learning such a complex real-world distribution may be a burdensome task to a single CNN. The distribution of images in real-world situations is very diverse, depending on some criteria, such as exposure, camera manufacturers, capturing environments, etc. Also, the additional prior information such as noise level is unavailable, limiting the training scheme within the naïve blind model.

To address the above issues, we propose a new method that can handle blind scenarios, namely Variational Deep Image Restoration (VDIR). Our approach is universal, as it can be adopted for generic image restoration problems. We split the objective of a given image restoration task into simpler sub-problems based on variational approximation, which eventually eases the overall task. Specifically, we provide efficient prior information to the restorer to accurately infer the posterior distribution. For this, we first seek efficient prior information based on the Bayesian perspective and try to approximate posteriors based on our approximated variational distribution.

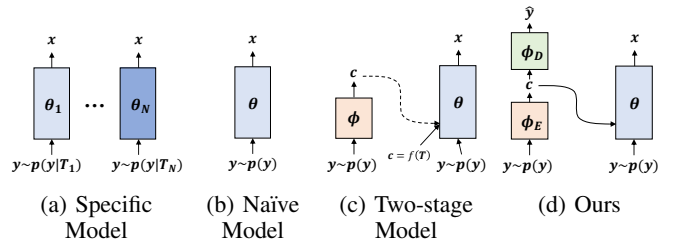


Fig. 1: Categories of image restoration frameworks.

In summary, our contributions are as follows.

- We propose an end-to-end trainable CNN, which can be universally applied to blind and real-world image restoration tasks.
- Based on variational approximation, we tackle the image restoration problem by relaxing the original problem into easier sub-problems.
- We seek to find efficient prior information that incorporates both task- and domain-relevant information.
- We have shown that the proposed method achieves state-of-the-art performances in several image restoration tasks, such as AWGN image denoising, real-noise denoising, blind super-resolution, and JPEG compression artifacts reduction.

## II. RELATED WORK

In this section, we categorize previous CNN-based image restoration methods according to the target objectives. Then, we further discuss prior information that is exploited in previous methods. For the entire paper,  $p_{data}(\cdot)$  denotes the underlying data distribution.

### A. Specific Non-blind Model

The early CNN-based image restoration methods [11], [13], [15], [16], [19], [58], [59] adopted “specific non-blind model,” which is a separate network parameterized by  $\theta_i$  and trained for a specific degradation  $T_i$ , as shown in Fig. 1a. Its target objective can be expressed as

$$\hat{\theta}_i = \arg \max_{\theta_i} \mathbb{E}_{p_{data}(\mathbf{x}, \mathbf{y}, \mathbf{c})} [\log p_{\theta_i}(\mathbf{x} | \mathbf{y}, \mathbf{c}_i)] \quad (4)$$

where  $\mathbf{c}_i$  is a function of  $T_i$ , e.g., the noise level for denoising, blur kernels or scaling factors for super-resolution, the quality factor for compression artifacts reduction, etc. The non-blind approaches have limitations in practical use because we need to know or accurately estimate the degradation information, which is generally not an easy problem. Also, we need to prepare many networks in the bag to cope with large variations of degradation in the real world, requiring too large memories.

### B. Naïve Blind Model

Most of the blind methods are in the category of naïve blind model, which rely only on the representation power of CNN, as described in Fig. 1b. For example with denoising, since there is no prior information such as noise level in real-world

noisy images, it would be an appropriate approach to adopt the naïve blind model. The target objective is expressed as

$$\hat{\theta} = \arg \max_{\theta} \mathbb{E}_{p_{data}(\mathbf{x}, \mathbf{y})} [\log p_{\theta}(\mathbf{x}|\mathbf{y})], \quad (5)$$

for training a single network parameterized by  $\theta$  to capture the conditional distribution. In general, naïve blind models show worse performance than the specific ones [11], [36], [60], since the marginal posterior  $p(\mathbf{x}|\mathbf{y})$  is more complicated than the posterior given the degradation,  $p(\mathbf{x}|\mathbf{y}, T)$ . Specifically, several methods such as [11], [37], [42], [55], [56], [61] come under this category.

### C. Two-Stage Blind Model

Some recent methods can be categorized as a two-stage blind model, where the degradation parameters  $\mathbf{c}$ , which is a function of  $T$ , are first estimated and then fed to the restoration network along with the input image. Its target objective is

$$\hat{\phi} = \arg \max_{\phi} \mathbb{E}_{p_{data}(\mathbf{y}, \mathbf{c})} [\log p_{\phi}(\mathbf{c}|\mathbf{y})], \quad (6)$$

$$\hat{\theta} = \arg \max_{\theta} \mathbb{E}_{p_{data}(\mathbf{x}, \mathbf{y}, \mathbf{c})} [\log p_{\theta}(\mathbf{x}|\mathbf{y}, \mathbf{c})], \quad (7)$$

where  $\phi$  and  $\theta$  denote the parameters of the estimator and the restorer, respectively. For the Gaussian denoising,  $\mathbf{c}$  is selected as the standard deviation of Gaussian distribution [12], [26], [29], and for the real-noise, more complicated parameters are selected [28], [38], [62]. For super-resolution, blur kernel is selected [17], [21]–[23], and quality factor is selected for JPEG compression artifacts reduction [20]. Note that prior information on the degradation model is additionally required for this setting.

### D. Additional Prior Information

For developing deep learning-based image/video restoration algorithms, many kinds of prior information have been considered to better help the network learn such complicated problems. Mainly, the task-relevant priors and the domain-relevant priors are considered.

Typically, the task-relevant priors such as the degradation model with its parameters are widely used [12], [17], [20], [29]. On the other hand, the domain-relevant priors, which have long been considered from traditional image restoration, have also been considered. For example, natural image priors such as non-local self-similarity [13], [18], [63] or sparsity by wavelet transforms [64]–[66] are additionally provided to the network or incorporated in a somewhat different way by conditioning the network architectures. Semantic information is also utilized to guide the rebuilding of high-frequency details in super-resolution tasks [32]. Even more, the facial domain-specific priors are used for the face-specified super-resolution. For example, facial landmarks or heatmaps are exploited for face super-resolution in [67], [68]. For video restoration problems, the main domain-relevant prior may be temporal coherency, and some of the methods use optical-flow as the domain-relevant prior [69]–[73]. Note that these approaches aim at specific tasks which cannot be applied to generic image restoration problems, and the pre-designed priors are often sub-optimal [72].

Besides, there have been other priors exploited for image restoration tasks. It has been noticed that residual networks, which bypass diverse levels of information within the network, can be considered a way of providing additional priors to each inner block of the network [74]. However, it is mainly related to architectural design, and any constraints on the residual information are imposed while training. Very recently, deep generative priors based on pre-trained GAN models [75], [76] have been proposed in [77]–[79]. The prior information encapsulated in a pre-trained GAN shows dramatic improvements in image restoration tasks, but their performance gains mostly rely on the pre-trained networks and external dataset. Moreover, most pre-trained GANs (StyleGAN [75]) are trained with datasets in a specific category such as face or cat. Therefore, available image categories are limited. Also, auxiliary supervision on residual image works as a prior for dynamic scene deblurring [80]. However, the prior is a reconstruction of the residual, and the essential part of the above-stated work is a meta-learning step that requires gradient descent updates for inference. On the other hand, our VDIR does not require any supervision on the external dataset or the pre-trained network, and the prior is jointly learned while training. Also, only a feed-forward pass is required to tune the behavior of the restoration network.

## III. VARIATIONAL DEEP IMAGE RESTORATION

This section presents our target objective regarding the inference of the high-quality image  $\mathbf{x}$  and the latent prior information  $\mathbf{c}$ , then reformulates the problem to tractable sub-problems.

### A. Problem Statement

For a given low-quality image  $\mathbf{y}$ , the objective is to find a latent high-quality image  $\mathbf{x}$ , which is described as a MAP inference problem in eq. (2). To solve this problem, we start from a different perspective compared to former MAP frameworks.

Let us first consider the joint distribution  $p(\mathbf{x}, \mathbf{y})$  and describe a framework that generates the low and high-quality images. Our goal is to learn underlying joint distribution and further infer the posterior distribution  $p(\mathbf{x}|\mathbf{y})$  from the joint distribution. For this, we introduce a new latent random variable  $\mathbf{c}$  in this framework, which implies both domain- and task-relevant properties. In our framework, we assume that the low-quality images are generated based on a procedure involving  $\mathbf{c}$ , which can be split into three processes: (1) given a domain prior  $\kappa$  and a degradation  $T$ , the latent variable  $\mathbf{c}$  is generated from some conditional distribution  $p(\mathbf{c}; \kappa, T)$ , (2) from  $\mathbf{c}$  and a natural image prior  $\xi$ , a high-quality natural image is generated from  $p(\mathbf{x}|\mathbf{c}; \xi)$ , and (3) from  $\mathbf{x}$  and  $\mathbf{c}$ , a low-quality degraded image is generated from  $p(\mathbf{y}|\mathbf{x}, \mathbf{c})$ .

In this framework, we bring a new inference problem of the posterior  $p(\mathbf{c}|\mathbf{x}, \mathbf{y})$ , where the latent  $\mathbf{c}$  includes both domain- and task-relevant information through the given information of high- and low-quality images. However, this inference problem is intractable. Also, our other objective is to infer  $\mathbf{x}$ , which cannot be observed during the inference.

In summary, our inference problems of interest are

- the inference of  $\log p(\mathbf{c}|\mathbf{x}, \mathbf{y})$ , and
- the inference of  $\log p(\mathbf{x}|\mathbf{y})$ ,

which are approximated and solved by training CNNs with appropriate datasets for the given inference problems.

### B. Proposed Variational Lower Bound

To approximate the posterior  $p(\mathbf{c}|\mathbf{x}, \mathbf{y})$ , we introduce a tractable probability distribution  $q(\mathbf{c}|\mathbf{y})$ . Then, the joint probability distribution  $\log p(\mathbf{x}, \mathbf{y})$  can be reformulated as

$$\begin{aligned} \log p(\mathbf{x}, \mathbf{y}) = & \mathbb{E}_{\mathbf{c} \sim q(\mathbf{c}|\mathbf{y})} [\log p(\mathbf{x}|\mathbf{y}, \mathbf{c})] \\ & + D_{KL}(q(\mathbf{c}|\mathbf{y})||p(\mathbf{c}|\mathbf{x}, \mathbf{y})) \\ & - D_{KL}(q(\mathbf{c}|\mathbf{y})||p(\mathbf{c})) \\ & + \mathbb{E}_{\mathbf{c} \sim q(\mathbf{c}|\mathbf{y})} [\log p(\mathbf{y}|\mathbf{c})], \end{aligned} \quad (8)$$

with some prior distribution  $p(\mathbf{c})$ . The details of the derivation can be found in the *supplemental material*. To approximate the intractable KL divergence term between  $q(\mathbf{c}|\mathbf{y})$  and  $p(\mathbf{c}|\mathbf{x}, \mathbf{y})$ , we introduce a *variational lower bound*  $\mathcal{L}$ .

**Definition 1** Variational lower bound  $\mathcal{L}$  is defined as

$$\begin{aligned} \mathcal{L} = & \mathbb{E}_{\mathbf{c} \sim q(\mathbf{c}|\mathbf{y})} [\log p(\mathbf{x}|\mathbf{y}, \mathbf{c})] \\ & - D_{KL}(q(\mathbf{c}|\mathbf{y})||p(\mathbf{c})) + \mathbb{E}_{\mathbf{c} \sim q(\mathbf{c}|\mathbf{y})} [\log p(\mathbf{y}|\mathbf{c})]. \end{aligned} \quad (9)$$

**Theorem 1** Given a low-quality image  $\mathbf{y}$  and its underlying high-quality image  $\mathbf{x}$ , the joint log-distribution  $\log p(\mathbf{x}, \mathbf{y})$  can be reformulated including variational lower bound  $\mathcal{L}$  as

$$\log p(\mathbf{x}, \mathbf{y}) = \mathcal{L} + D_{KL}(q(\mathbf{c}|\mathbf{y})||p(\mathbf{c}|\mathbf{x}, \mathbf{y})). \quad (10)$$

Then,

$$\log p(\mathbf{x}, \mathbf{y}) \geq \mathcal{L}. \quad (11)$$

The proof of eq. (10) is straightforward from eqs. (8) and (9). Also, eq. (11) comes from the fact that the KL divergence in eq. (10) is non-negative.

**Definition 2** We also define a log-posterior  $q(\mathbf{x}|\mathbf{y})$  which approximates the original posterior  $p(\mathbf{x}|\mathbf{y})$  as

$$\begin{aligned} q(\mathbf{x}|\mathbf{y}) &= \int_{\mathbf{c}} q(\mathbf{x}, \mathbf{c}|\mathbf{y}) d\mathbf{c} \\ &= \int_{\mathbf{c}} p(\mathbf{x}|\mathbf{y}, \mathbf{c}) q(\mathbf{c}|\mathbf{y}) d\mathbf{c}. \end{aligned} \quad (12)$$

Then, the MAP inference given  $\mathbf{y}$  can be done by  $\arg \max_{\mathbf{x}} \log q(\mathbf{x}|\mathbf{y})$ .

Through our reformulation, maximizing the likelihood of the joint probability distribution is approximated as to maximize our *variational lower bound*. Notably, the first term of  $\mathcal{L}$  in eq. (9) is the only term relevant to the relation between  $\mathbf{x}$  and  $\mathbf{y}$ , responsible for image restoration. The other terms are regularization terms, which impose constraints on the latent variable  $\mathbf{c}$ . The second term is the KL divergence, which constrains the latent distribution, and the third term is the auto-encoder reconstruction term of the low-quality images.

As neural networks are experts at inference, in an amortized way [81], [82], we employ three CNNs parameterized by  $\theta$ ,

$\phi_E$ , and  $\phi_D$  for the variational inference. Specifically, our final objective is

$$\begin{aligned} \arg \max_{\theta, \phi_E, \phi_D} \mathbb{E}_{p_{data}(\mathbf{x}, \mathbf{y})} [ & \mathbb{E}_{\mathbf{c} \sim q_{\phi_E}(\mathbf{c}|\mathbf{y})} [\log p_{\theta}(\mathbf{x}|\mathbf{y}, \mathbf{c})] \\ & - D_{KL}(q_{\phi_E}(\mathbf{c}|\mathbf{y})||p(\mathbf{c})) \\ & + \mathbb{E}_{\mathbf{c} \sim q_{\phi_E}(\mathbf{c}|\mathbf{y})} [\log p_{\phi_D}(\mathbf{y}|\mathbf{c})]], \end{aligned} \quad (13)$$

with underlying empirical data distribution  $p_{data}(\mathbf{x}, \mathbf{y})$ . By introducing such regularizations, our restorer can approximately solve a MAP problem according to the latent  $\mathbf{c}$ , where  $\mathbf{c}$  is the variable involved in the low-quality image generation process, which involves both task- and domain-relevant prior information. In other words, our restorer divides the problem according to the latent vector  $\mathbf{c}$ , where  $\mathbf{c}$  should “imply” the low-quality image manifold.

### C. Corresponding Loss Terms

**First Term** The first term means to estimate  $\mathbf{x}$  conditioned on  $\mathbf{y}$  and  $\mathbf{c}$ . If there is a function (network) that performs this as  $\hat{\mathbf{x}} = f(\mathbf{y}, \mathbf{c})$ , then the problem is to train the network to minimize the difference between  $\mathbf{x}$  and  $\hat{\mathbf{x}}$ . We adopt L1 loss between the ground-truth clean image and the inferred output to minimize the distortion based on the i.i.d. Laplacian prior. We denote the corresponding loss term as  $\mathcal{L}_{res}$ :

$$\mathcal{L}_{res} = \|\mathbf{x} - \hat{\mathbf{x}}\|_1, \quad (14)$$

where  $\hat{\mathbf{x}} = f(\mathbf{y}, \mathbf{c})$  as stated above, and  $f(\mathbf{y}, \mathbf{c})$  is our main restoration network that will be explained in Sec. IV.E, with Fig. 3.

**Second Term** The second term measures the fidelity of  $\mathbf{c}$  extracted through the encoder  $\phi_E$  with the input  $\mathbf{y}$ , and this is represented as the KL divergence between  $q_{\phi_E}(\mathbf{c}|\mathbf{y})$  and  $p(\mathbf{c})$ . The KL divergence between the prior distribution and the posterior can be calculated analytically. Since  $p(\mathbf{c})$  is a modeling of the latent distribution, any parametric distribution model can be used [83], [84], and we use a standard Gaussian for simplicity and convenience. Specifically, we set the prior  $p(\mathbf{c})$  as Gaussian distribution with zero mean and unit covariance. Thus, the KL divergence term is

$$\begin{aligned} D_{KL}(\mathcal{N}(\mu, \Sigma)||\mathcal{N}(0, I)) \\ = \frac{1}{2} [-\log \det(\Sigma) - n + \text{tr}(\Sigma) + \mu^T \mu], \end{aligned} \quad (15)$$

$$D_{KL}(q(\mathbf{c}|\mathbf{y})||p(\mathbf{c})) = \frac{1}{2} \left[ \sum_{i=1}^n (-\log \sigma_i^2 - 1 + \sigma_i^2 + \mu_i^2) \right],$$

where  $n$  is the dimension of the random variable.

**Third Term** In the case of the third term, which is the auto-encoder reconstruction term, we may also adopt L1 loss between the noisy image  $\mathbf{y}$  and the decoder’s output  $\hat{\mathbf{y}}$ , like in the first term. However, using only pixel-wise loss strictly assumes  $p(\mathbf{y}|\mathbf{c})$  to be a family of the probability distribution of i.i.d. Laplacian or Gaussian. Hence, we additionally adopt adversarial loss [30] to relax and better learn the low-quality image distribution. Specifically, we adopt non-saturating GAN

loss [30], corresponding to minimizing Jensen-Shannon divergence between  $p_{data}(\mathbf{y})$  and  $p_{\phi_D}(\mathbf{y}|\mathbf{c})$ . It is expressed as

$$\mathcal{L}_D = -\log D(\mathbf{y}) - \log(1 - D(\hat{\mathbf{y}})), \quad (16)$$

$$\mathcal{L}_{adv} = -\log D(\hat{\mathbf{y}}) \quad (17)$$

where  $\mathcal{L}_D$  and  $\mathcal{L}_{adv}$  denote the discriminator loss and the adversarial loss, respectively. For each specific task, we may inject known priors if available. In this case, we add an estimation loss so that the latent space learns the known degradation information. Eventually, the latent  $\mathbf{c}$  works as an additional prior for the restorer, which contains an abstract of the low-quality image distribution.

With the above notions, the loss  $\mathcal{L}_{rec}$  for the third term is described as

$$\mathcal{L}_{rec} = \|\mathbf{y} - \hat{\mathbf{y}}\|_1 + \lambda_1 \mathcal{L}_{adv} + \lambda_2 \|f(T) - EST(\mathbf{c})\|_1, \quad (18)$$

where  $EST(\cdot)$  is a simple two-layer CNN (conv-relu-conv).  $f(T)$  is an injected prior knowledge when available.  $T$  and  $f(T)$  are symbolic expressions, where  $T$  stands for a kind of degradation and  $f(T)$  is defined differently depending on the restoration tasks. In the following sections, we will show examples of  $f(T)$  for Gaussian denoising, super-resolution, and compression artifacts reduction. When we do not have the knowledge, we do not use it by setting  $\lambda_2 = 0$ .

**Overall Loss** The overall loss is the sum of three terms where normalized KL divergence is used and multiplied by  $\beta$  [84]. Then, the final objective is

$$\arg \min_{\theta, \phi_E, \phi_D} \mathbb{E}_{p_{data}(\mathbf{x}, \mathbf{y})} [\mathcal{L}_{res} + \beta D_{KL} + \mathcal{L}_{rec}]. \quad (19)$$

## IV. DISCUSSIONS

### A. Difference from VDN

Both our VDIR and VDN [28] adopt variational framework for image denoising or image restoration problem. However, there are mainly three differences. First, VDN models the noise distribution with non-i.i.d Gaussian distribution, but ours does not explicitly model the distribution, instead it is implicitly learned through the network. Second, VDN sets the latent variable as latent clean image  $\mathbf{z}$  and approximates the distribution over the noisy observation  $\mathbf{y}$ :  $\log p(\mathbf{y})$ . On the other hand, our method introduces the latent variable  $\mathbf{c}$  containing beneficial information and approximates the joint distribution of both  $\mathbf{x}$  and  $\mathbf{y}$ :  $\log p(\mathbf{x}, \mathbf{y})$ . Lastly, VDN analytically solves the likelihood function, whereas our method uses a neural network to approximate likelihood.

### B. Difference from Plug-and-play based methods

Diverse plug-and-play based methods also utilize priors for image restoration [24], [85]–[88]. However, there are two main differences compared to ours. First, the approach and modeling of the target objective function are different. Plug-and-play methods start their formulation based on the MAP framework and explicitly divide the posterior term into the data fidelity term and the prior term. Then, they carefully deal with each term. On the other hand, our method directly learns the posterior based on the variational approximation with implicit

prior. Second, the plug-and-play methods are iterative due to their inherent nature of optimization. Although the priors are learned from the dataset, several iterations are required to obtain desirable results. On the contrary, our method requires one feed-forward pass to obtain restored results, which is efficient regarding the computational complexity.

### C. Probabilistic View

In this subsection, we discuss our method with other frameworks with the probabilistic perspective. Let us assume the restoration loss term as L2-norm for simplicity, which assumes i.i.d. Gaussian distribution as target probabilistic family (L1-norm is associated with Laplacian distribution). We refer a neural network parameterized by  $\theta$  as  $f_\theta(\cdot)$ .

The naïve blind model which models  $p_\theta(\mathbf{x}|\mathbf{y}) = \mathcal{N}(f_\theta(\mathbf{y}), I/2)$ , and learning the data distribution under this family hinders expressiveness. Since the posterior distribution  $p(\mathbf{x}|\mathbf{y})$  including diverse degradation is too complex to be captured by a single Gaussian, its performance cannot be expected as much as the specific model with simpler  $p(\mathbf{x}|\mathbf{y})$  with a single degradation.

On the other hand, our framework models  $p(\mathbf{x}|\mathbf{y}, \mathbf{c}) = \mathcal{N}(f_\theta(\mathbf{y}, \mathbf{c}), I/2)$ . It is still Gaussian but learns different mean values with respect to  $\mathbf{c}$ , which grants more representation power for learning multiple Gaussians in accordance with  $\mathbf{c}$ . (Analogous to the relation between Gaussian and Gaussian mixture model.) Then, the marginal posterior has more representative powers  $p(\mathbf{x}|\mathbf{y}) = \int_{\mathbf{c}} p(\mathbf{x}|\mathbf{y}, \mathbf{c})p(\mathbf{c}|\mathbf{y})d\mathbf{c}$ . Though, our inference approximates the marginal posterior through Monte-Carlo using only one sample of  $\mathbf{c}$ .

The two-stage model can be considered a special case of our method where the  $q(\mathbf{c}|\mathbf{y})$  is chosen as deterministic. In this case, the  $\mathbf{c}$  is determined based on the prior knowledge and carefully modeled by “understanding the data.” Then, the point estimate of  $\hat{\mathbf{c}} = \arg \max_{\mathbf{c}} q(\mathbf{c}|\mathbf{y})$  is used for the second step inference [29]. Note that this bi-level optimization scheme would be sub-optimal to the task objective, compared to the joint optimization. Unlike the two-stage model, our method is more Bayesian and implicitly learns  $\mathbf{c}$ , which is enforced to contain the degradation information along with the original image content information. In other words, our method conducts Bayesian inference, whereas the two-stage model conducts deterministic estimates. Also, the additional information  $\mathbf{c}$  is learned by enforcing the network to “understand the data.”

### D. Discussions on Loss Terms

When we use only the first term, it is just a naïve approach to solve a blind restoration problem, totally relying on the discriminative power of CNN. In this case, the objective is

$$\arg \max_{\theta, \phi_E} \mathbb{E}_{p_{data}(\mathbf{x}, \mathbf{y})} [\mathbb{E}_{\mathbf{c} \sim q_{\phi_E}(\mathbf{c}|\mathbf{y})} [\log p_\theta(\mathbf{x}|\mathbf{y}, \mathbf{c})]]. \quad (20)$$

Note that no matter what latent distribution  $q_{\phi_E}(\mathbf{c}|\mathbf{y})$  we choose, this criteria is maximized if for each  $\mathbf{c}$ ,  $\mathbb{E}_{p_{data}(\mathbf{x}, \mathbf{y})} [\log p_\theta(\mathbf{x}|\mathbf{y}, \mathbf{c})]$  is maximized. In other words, there is a trivial solution “independent” to  $\mathbf{c}$ , if our model has the optimal parameter satisfying  $\theta^* =$

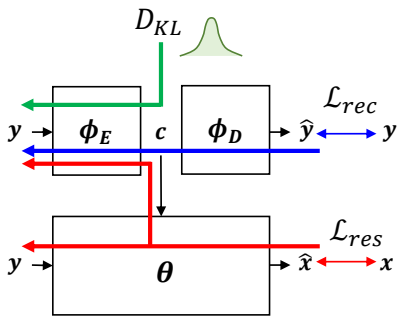
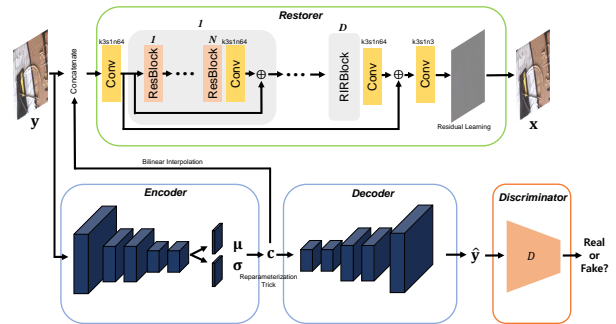


Fig. 2: Overall gradient flows of the loss terms.

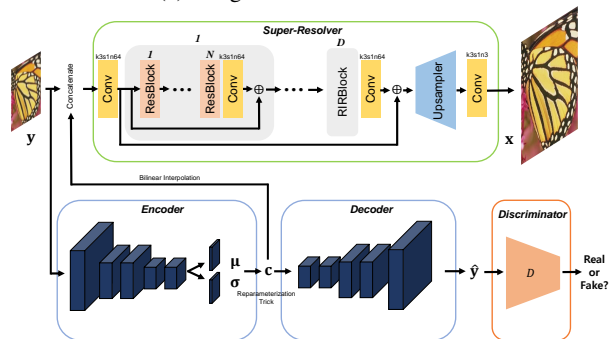
$\arg \max_{\theta} \mathbb{E}_{p_{data}(x,y)} [\log p_{\theta}(x|y)]$ . In this case,  $c$  collapses and the original problem cannot be divided into sub-problems. The second term gives regularization constraints. The KL divergence term forces the disentanglement of  $c$ , giving *discriminative power* over observed images  $y$ . The third term further gives constraints on the latent variable  $c$ . As the auto-encoder reconstruction term forces the reconstruction from  $c$  to  $y$ , this term forces  $c$  to include the information of the degraded image. Importantly, as in Fig. 2 that shows the gradient flow of each loss term, the encoder learns not only the reconstruction of the low-quality image (blue flow) but also the information suitable for image restoration (red flow) regularized to a specific probabilistic model through KL divergence (green flow). Also, it is trained in an end-to-end manner to let all the information be well reflected to the latent variable.

### E. Network Architecture

The overall network architecture is shown in Fig. 3. We present two architectures for the generic image restoration and the super-resolution, where the latter is slightly modified from the former. The restorer takes a low-quality image  $y$  with the latent variable  $c$  concatenated along the channel axis to infer the high-quality image  $x$ . The restorer is fully convolutional, thus highly scalable. For the restorer, the residual block (ResBlock) is adopted as the basic building block [16], [89]. Precisely, the same residual block of [16] is adopted, which consists of a  $3 \times 3$  convolution layer with 64 filters followed by the rectified linear unit (ReLU) and another convolution layer (Conv-ReLU-Conv). Then, the input is added to the output of the convolution layer, which forms the skip-connection. The  $N$  residual blocks and one convolution layer compose the residual-in-residual block (RIRBlock) [58]. The restorer consists of  $D$  RIRBlocks with some convolution layers and a long skip-connection, as shown in Fig. 3a. The last convolution layer infers the residual image instead of the high-quality image itself, according to [11]. The latter part of the restorer is slightly modified for super-resolver. As the spatial feature size is different between  $x$  and  $y$  for the super-resolution, instead of the residual learning, we adopt post-upsampler at the latter part as shown in Fig. 3b. The upsampler is a sub-pixel convolution layer that consists of a convolution layer followed by a sub-pixel shuffler [90].



(a) Image Restoration Network



(b) Super-Resolution Network

Fig. 3: The overall architecture of proposed VDIR, where  $k$ ,  $s$ , and  $n$  denote kernel size, stride, and the number of filters, respectively. Image restoration network is adopted for the image denoising and compression artifacts reduction tasks, while the super-resolution network is employed for a super-resolution task. Note that the decoder is not used for the inference. The structure of the discriminator is shown in the supplementary material.

The encoder and decoder networks are simple feedforward convolutional networks without skip-connection. The encoder decreases the feature map's spatial size twice (one-fourth of its height and width), and the output  $c$  has four channels. For the differentiable Monte Carlo, we adopt the reparameterization trick [83], [84]. The decoder network has symmetrical architecture as the encoder. The details of the encoder, decoder, and discriminator architectures are presented in the *supplemental material*.

### F. Implementation Details

For our VDIR, we set  $N = 5$  and  $D = 5$ , which amounts to about  $2.2M$  parameters, including the restorer and the encoder. We adopt Adam optimizer with  $\beta_1 = 0.9$  and  $\beta_2 = 0.999$  with initial learning rate  $2 \times 10^{-4}$ . The learning rate is decayed by half in every 100,000 iterations, until it reaches  $2 \times 10^{-5}$ .

## V. IMAGE DENOISING

We perform two image denoising tasks: blind AWGN image denoising and real-noise denoising.



TABLE I: The average PSNR on AWGN denoising. The best results are highlighted in red and the second best in blue.

Noise level	Dataset	CBM3D [8]	CDnCNN [11]	FFDNet [12]	UNLNet [37]	VDN [28]	VDIR (Ours)
$\sigma = 10$	CBSD68	35.91	36.13	36.14	36.20	36.29	36.34
	Kodak24	36.43	36.46	36.69	-	36.85	37.02
	Urban100	36.00	34.61	35.78	-	35.97	36.30
$\sigma = 30$	CBSD68	29.73	30.34	30.32	30.21	30.64	30.64
	Kodak24	30.75	31.17	31.27	31.18	31.67	31.74
	Urban100	30.36	30.00	30.53	30.41	31.14	31.41
$\sigma = 50$	CBSD68	27.38	27.95	27.97	27.85	28.33	28.33
	Kodak24	28.46	28.83	28.98	28.86	29.44	29.49
	Urban100	27.94	27.59	28.05	27.95	28.86	29.10
$\sigma = 70$	CBSD68	26.00	25.66	26.55	-	26.93	26.94
	Kodak24	27.09	26.36	27.56	-	28.05	28.10
	Urban100	26.31	25.24	26.40	-	27.31	27.55

TABLE II: Results on SIDD [40] benchmark. The best results are highlighted in red and the second best in blue.

Method	Blind/Non-blind	Parameters	PSNR	SSIM
BM3D [8]	Non-blind	-	25.65	0.685
WNNM [7]	Non-blind	-	25.78	0.809
DnCNN [11]	Non-blind	668 K	23.66	0.583
TNRD [91]	Non-blind	27 K	24.73	0.643
CBDNet [38]	Blind	4.4 M	33.28	0.868
RIDNet [42]	Blind	1.5 M	38.71	0.914
VDN [28]	Blind	7.8 M	39.26	0.955
AINDNet+TF [62]	Blind	13.7 M	38.95	0.952
MIRNet [92]	Blind	31.8 M	39.72	0.959
MPRNet [93]	Blind	15.7 M	39.71	0.958
InvDN [94]	Blind	2.6 M	39.28	0.955
VDIR (Ours)	Blind	2.2 M	39.26	0.955
VDIR+ (Ours)	Blind	2.2 M	39.33	0.956

A. Results on AWGN Denoising

For the synthetic Gaussian noise, we train with DIV2K [96] dataset which includes 800 high-resolution images, and add synthetic Gaussian noise with noise level  $\sigma \in [5, 70]$ . We extract  $96 \times 96$  patches and the batch size is set to 16. We set  $\beta = 0.01$  and  $\lambda_2 = 1$  for the hyperparameters, and  $\sigma = f(T)$  to impose our prior knowledge, letting  $c$  to include the noise level information. The performance is evaluated with three color-image datasets: CBSD68 [97], Kodak24, and Urban100 [98] with noise levels  $\sigma = 10, 30, 50, 70$ . We compare our method with several AWGN denoising methods: CBM3D [8], DnCNN [11], FFDNet [12], UNLNet [37], and VDN [28]. The results are presented in TABLE I. The visualized results for the AWGN denoising and all the following experiments are provided in the *supplemental material*.

Note that CBM3D [8] and FFDNet [12] are non-blind methods, whereas the rest are blind ones. In most cases, our

TABLE III: Results on DND [41] benchmark. The best results are highlighted in bold.

Method	Blind/Non-blind	Parameters	PSNR	SSIM
BM3D [8]	Non-blind	-	34.51	0.8507
WNNM [7]	Non-blind	-	34.67	0.8646
DnCNN+ [11]	Non-blind	668 K	37.90	0.9430
FFDNet+ [12]	Non-blind	825 K	37.61	0.9415
GCBD [55]	Blind	561 K	35.58	0.9217
CBDNet [38]	Blind	4.4 M	38.06	0.9421
RIDNet [42]	Blind	1.5 M	39.26	0.9528
VDN [28]	Blind	7.8 M	39.38	0.9518
AINDNet(S) [62]	Blind	13.7 M	39.53	0.9561
MIRNet [92]	Blind	31.8 M	39.88	0.9563
MPRNet [93]	Blind	15.7 M	39.80	0.9540
InvDN [94]	Blind	2.6 M	39.57	0.9522
VDIR (Ours)	Blind	2.2 M	39.63	0.9528
VDIR+ (Ours)	Blind	2.2 M	39.69	0.9532

VDIR shows the best results but requires a smaller number of parameters (2.2 M) compared to the second-best VDN [28] (7.8 M). In conclusion, the results show that our VDIR surpasses other methods considering the tradeoff between the performance and the network capacity (the number of parameters).

B. Results on Real-Noise Denoising

For the real-world camera noise, we train the network using two datasets: Smartphone Image Denoising Dataset (SIDD) [40] and DIV2K [96], along with realistic synthetic noise [38]. SIDD is a collection of pairs of noisy and clean images from five smartphone cameras. It consists of 320 image pairs for training. For synthetic noise, we adopt the noise synthesis process of CBDNet [38], where the camera pipeline, including demosaicking and camera response functions, and

TABLE IV: The average PSNR/SSIM results of blind super-resolution for scaling factor  $\times 2$ . The best results are highlighted in **bold**.

Kernel	Dataset	Bicubic	RCAN [58]	IKC [17]	MZSR [23]	DIP-FKP [95] + USRNet [24]	VDIR (Ours)
$g_{2.0}^d$	Set5	28.73/0.8449	29.15/0.8601	29.05/0.8896	36.05/0.9439	30.65/0.8861	<b>36.95/0.9506</b>
	BSD100	26.51/0.7157	26.89/0.7394	27.46/0.8156	31.09/0.8739	27.56/0.7484	<b>31.57/0.8815</b>
	Urban100	23.70/0.7109	24.14/0.7384	25.17/0.8169	29.19/0.8838	25.96/0.7878	<b>30.10/0.8987</b>
$g_{ani}^d$	Set5	28.15/0.8265	28.42/0.8379	28.74/0.8565	34.78/0.9323	29.32/0.8694	<b>36.25/0.9469</b>
	BSD100	26.00/0.6891	26.22/0.7062	26.44/0.7310	29.54/0.8297	26.78/0.7222	<b>30.51/0.8594</b>
	Urban100	23.13/0.6796	23.35/0.6982	23.62/0.7239	27.34/0.8369	24.86/0.7517	<b>28.58/0.8720</b>

TABLE V: The average PSNR/SSIM results of blind super-resolution for scaling factor  $\times 4$ . Isotropic Gaussian kernel  $g_{2.0}^d$  is used for the blur kernel. The best results are highlighted in **bold**.

Dataset	Bicubic	RCAN [58]	IKC [17]	MZSR [23]	DIP-FKP [95] + USRNet [24]	VDIR (Ours)
Set5	24.74/0.7321	23.92/0.7283	24.01/0.7322	30.50/0.8704	28.14/0.8427	<b>31.46/0.8884</b>
BSD100	24.01/0.5998	23.16/0.5918	23.12/0.5939	26.89/0.7168	25.64/0.6720	<b>27.27/0.7271</b>
Urban100	21.16/0.5811	19.52/0.5400	19.81/0.5583	24.65/0.7394	23.62/0.7102	<b>25.62/0.7730</b>

heteroscedastic Gaussian noise are considered to mimic real-noise as much as possible. We extract  $256 \times 256$  patches with the batch size 4 for training. We set  $\beta = 0.01$  and  $\lambda_2 = 0$ , since we do not have the degradation information for the real-noise case. We compare with several image denoising methods: BM3D [8], WNNM [7], DnCNN [11], TNRD [91], FFDNet [12], GCBD [55], CBDNet [38], RIDNet [42], VDN [28], AINDNet [62], MIRNet [92], MPRNet [93], and InvDN [94]. For the evaluation, we use two widely used real-world image denoising benchmarks.

- **SIDD**: SIDD provides 1,280 small patches for validation and 1,280 for test, which are visually similar to training images. Ground-truth patches for the validation set are provided but not for the test set.
- **DND**: Darmstadt Noise Dataset (DND) consists of 50 images with real-noise from 50 scenes from four consumer cameras. Then, the images are further cropped by the provider, which results in 1,000 small patches with a size of  $512 \times 512$ .

Both test sets do not provide the ground-truth image; therefore, the evaluation can only be performed through online submission.

Overall results on two benchmarks are listed in TABLE II and III. It is observed that our method shows comparable results to others, on both benchmarks in terms of PSNR and SSIM [99]. Note that we also demonstrate the results with self-ensemble [100], which is denoted with ‘+’ sign.

Compared to conventional methods such as BM3D [8] and WNNM [7], it is evident that the data-driven methods are superior in real-noise denoising due to the power of CNN and large-scale external dataset. Also, many assumptions and constraints in the conventional methods might have resulted in deteriorated performance. In the case of CNN-based methods for AWGN such as DnCNN [11] and FFDNet [12], they suffer from domain shift between i.i.d. Gaussian and real-noise. On the other hand, most of the recent CNN-based real image denoising methods [28], [38], [42], [62], [94] show

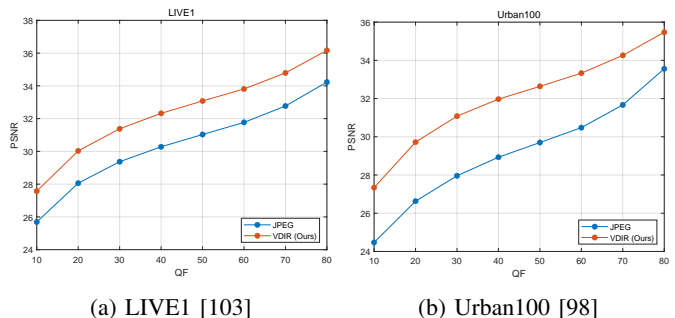


Fig. 4: PSNR vs. QF curves of artifacts reduction results on two datasets.

competitive results, achieving state-of-the-art performances.

For a fair comparison, we also denote the number of parameters for the CNN-based methods. Note that MIRNet [92] achieves PSNR gain against our method about 0.2 dB in DND, but the number of parameters is 31.8 M which exceeds an order of magnitude compared to ours. Also, the MPRNet [93] achieves higher performance (0.17 dB) using a larger network (15.7 M parameters). Since our method solves simpler sub-problems conditioned on the latent variable  $\mathbf{c}$ , it requires a smaller network than other denoising networks, which are the naïve models. In other words, the problem given to other methods is more complicated due to the difficulty of ill-posed real image denoising with diverse conditions. Therefore, our method achieves state-of-the-art performances in real-world image denoising with fewer network parameters than others.

## VI. BLIND IMAGE SUPER-RESOLUTION

To verify the generality of our method, we also evaluate our method on blind image super-resolution task following the settings of [23]. We train with DIV2K [96] dataset with various Gaussian kernels for blur kernels  $k \in \mathbb{R}^{15 \times 15}$  with the same setting of MZSR [23]. We adopt direct decimation



TABLE VI: The average PSNR/SSIM results on JPEG compression artifacts reduction. The best results are highlighted in **bold**. The numbers for compared methods are from the original papers, and the blank cells are not reported cases.

QF	Dataset	JPEG	AR-CNN [19]	Guo <i>et al.</i> [101]	MemNet [35]	Galteri <i>et al.</i> [102]	VDIR (Ours)
10	Classic5	27.82/0.7800	29.03/0.8108	29.62/0.8260	29.68/0.8282	-	<b>29.91/0.8333</b>
	LIVE1	27.77/0.7905	28.96/0.8217	29.36/0.8300	29.47/0.8337	29.45/0.8340	<b>29.56/0.8348</b>
	Urban100	26.33/0.8099	28.06/0.8515	29.01/0.9710	29.14/0.8741	-	<b>29.59/0.8803</b>
20	Classic5	30.12/0.8541	31.15/0.8691	31.77/0.8790	31.90/0.8658	-	<b>32.12/0.8850</b>
	LIVE1	30.07/0.8683	31.29/0.8871	31.68/0.8950	31.83/0.8973	31.77/0.8960	<b>31.95/0.8989</b>
	Urban100	28.57/0.8761	30.29/0.9024	31.39/0.9170	31.61/0.9206	-	<b>32.17/0.9257</b>
30	Classic5	31.48/0.8844	32.51/0.8963	33.04/0.9030	32.90/0.8988	-	<b>33.38/0.9066</b>
	LIVE1	31.41/0.9000	32.67/0.9161	33.09/0.9210	32.94/0.9169	33.15/0.9220	<b>33.38/0.9245</b>
	Urban100	30.00/0.9052	31.94/0.9279	32.90/0.9380	32.74/0.9348	-	<b>33.70/0.9437</b>
40	Classic5	32.43/0.9011	33.32/0.9098	33.89/0.9150	33.36/0.9060	-	<b>34.23/0.9187</b>
	LIVE1	32.35/0.9173	33.61/0.9303	34.09/0.9360	33.48/0.9248	34.09/0.9350	<b>34.37/0.9381</b>
	Urban100	31.07/0.9220	32.80/0.9391	33.98/0.9490	33.22/0.9405	-	<b>34.73/0.9535</b>
70	Classic5	34.98/0.9344	-	-	-	-	<b>36.40/0.9431</b>
	LIVE1	35.13/0.9512	-	-	-	-	<b>37.15/0.9638</b>
	Urban100	34.32/0.9563	-	-	-	-	<b>37.51/0.9723</b>
80	Classic5	36.44/0.9478	-	-	-	-	<b>37.63/0.9537</b>
	LIVE1	36.87/0.9641	-	-	-	-	<b>38.81/0.9733</b>
	Urban100	36.69/0.9697	-	-	-	-	<b>39.16/0.9796</b>

TABLE VII: The average PSNR results of JPEG compression artifacts reduction on sRGB color images.

Dataset	QF	10	20	30	40	50	60	70	80
LIVE1	JPEG	25.69	28.06	29.37	30.28	31.03	31.77	32.77	34.23
	VDIR	27.57	30.03	31.38	32.32	33.08	33.81	34.79	36.17
	$\Delta$ PSNR	1.88	1.97	2.01	2.04	2.05	2.04	2.02	1.94
Urban100	JPEG	24.47	26.63	27.96	28.93	29.70	30.48	31.67	33.56
	VDIR	27.34	29.72	31.08	31.97	32.64	33.33	34.26	35.47
	$\Delta$ PSNR	2.87	3.09	3.12	3.04	2.94	2.85	2.59	1.91

for sub-sampling method. Concretely, we extract  $48 \times 48$  as our low-resolution (LR) patches with the batch size 16 and trained two networks for each scaling factor:  $\times 2$  and  $\times 4$ . We set  $\beta = 0.01$ ,  $\lambda_2 = 1$ , and  $f(T) = k$  for the loss function. The evaluations are done in Y (luminance) channel of YCbCr colorspace, and two Gaussian kernels (isotropic and anisotropic) are considered for  $\times 2$ . Specifically,  $g_{2,0}^d$  denotes an isotropic Gaussian kernel with width 2.0 followed by direct subsampling.  $g_{ani}^d$  denotes an anisotropic Gaussian kernel with widths 4.0 and 1.0 and rotated with  $-0.5$  radian. The overall results are presented in TABLE IV and TABLE V.

We compare with several recent super-resolution methods: RCAN [58], IKC [17], MZSR [23], and DIP-FKP [95] with USRNet [24]. As shown in the tables, RCAN [58], which is a large model trained only for the bicubic downsampling scenario, suffers from domain shift, delivering inferior results to others. Blind super-resolution method such as IKC [17] shows improved results but still not plausible. MZSR [23], which

adopts a meta-learning strategy for fast adaptation, shows competitive results. Another blind super-resolution method, flow-based kernel prior [95] combined with USRNet [24] dubbed ‘‘DIP-FKP + USRNet’’ achieves plausible results. However, it is noteworthy that a thousand iterations are required to obtain a super-resolved image. Among all comparisons, our method outperforms others in the blind super-resolution task in terms of PSNR and SSIM.

## VII. JPEG COMPRESSION ARTIFACTS REDUCTION

We choose dominantly used JPEG [104] for the experiments on compression artifacts reduction. Specifically, we evaluate our method to reduce artifacts in images compressed by JPEG with a wide range of quality factors (QFs) in [10, 80]. We train with DIV2K [96] dataset with JPEG compression of MATLAB with QFs in [10, 80] with 10 intervals. In particular, we extract  $96 \times 96$  patches with the batch size 16 and we set  $\beta = 0.01$ ,  $\lambda_2 = 1$ , and  $f(T) = QF$  for the overall loss. We present two models: Y-model and RGB-model. Particularly, following the convention of previous works and for a fair comparison, we present a single channel model, which is for the Y channel of YCbCr colorspace. For more practical usage, we present a color model which is trained on sRGB images.

The performance is evaluated with three datasets: Classic5, LIVE1 [103], and Urban100 [98] with  $QF = 10, 20, 30, 40, 70, 80$ . We compare our method with other methods: AR-CNN [19], Guo *et al.* [101], MemNet [35], and Galteri *et al.* [102]. The results are shown in TABLE VI.

Most previous methods are targeting highly compressed images (low quality factors), and mostly are non-blind methods except MemNet [35]. It is observed from the table that our method can deal with a wide range of quality factors in a blind manner, and also it outperforms others with comparable model sizes. Importantly, many images we face every day online are JPEG, and their compression rates are very high (high QFs), but they still have undesirable artifacts. Previous methods did not deal with such images, for example, the quality factor above 70, but our method shows consistent PSNR/SSIM gain even on high quality factors of 70 and 80. For more practical application, we also present our color model results in TABLE VII and the performance curves in Fig. 4. Our VDIR shows consistent gains in the wide range of QFs with both datasets.

## VIII. ANALYSIS

### A. Analysis on the Latent Variable

In this subsection, we look into the latent space to investigate what kind of information is embedded.

1) *Latent Variable Manipulation*: First, to investigate the role of the latent variable  $\mathbf{c}$ , we manipulate the latent variable by feeding different inputs to the encoder of our AWGN denoiser. We feed the same noisy image with  $\sigma = 30$  to the denoiser and evaluate how the information encoded in  $\mathbf{c}$  affects the output image. The results are presented in Fig. 5. As the latent variable contains the information of the noisy image manifold, it provides an additional prior to the denoiser. As expected, the best result is obtained when  $\mathbf{c}$  is from the same noisy image (Fig. 5b). When  $\mathbf{c}$  is from the same image but with a lower noise level (Fig. 5d), the output still has the noise patterns because  $\mathbf{c}$  guides the noise level information. On the contrary, when  $\mathbf{c}$  is from the same image with a higher noise level (Fig. 5e), the resulting image is overly smoothed.

Additionally, we feed a flipped image of the noisy image to obtain  $\mathbf{c}$ , which has the same noise level but different contents (Fig. 5c). Notably, the PSNR drop is not as significant as the other cases, but some artifacts and degradation exist due to the difference in semantics. The noise is left in the building part, whereas the tree part is over-smoothed. Commonly, trees have more textures than buildings. The latent variable reflects such common knowledge and works as additional prior information that guides the denoiser and how much the noise should be removed.

We visualize the latent variable of each case in Fig. 6. It is observed that the latent variable reflects the content information along with the noise level information. Specifically, the values vary in accordance with the noise level, and also are different between the building and tree regions.

2) *t-SNE Visualization*: Secondly, we demonstrate t-SNE [105] visualization of  $\mathbf{c}$  in Fig. 7. In particular,  $\mathbf{c}$  is average-pooled to generate global abstract of a patch as  $AvgPool(\mathbf{c}) \in \mathbb{R}^n$ . We present results on 1,000 patches which are randomly extracted from DIV2K validation set, and the Gaussian noises are added with noise levels 10 to 55 at 5 intervals.

As shown in Fig. 7a, the latent embedding well represents the content information, generating clusters of similar-looking

TABLE VIII: Ablation study between two datasets: DND and SIDD

Dataset		Training	
		DIV2K	SIDD
Test	DND	39.37	39.37
	SIDD	35.04	39.22

patches. Also, the noise information is well embedded as shown in Fig. 7b, where the patches with similar noise levels are closely located, and the embedding varies continuously from low  $\sigma$  to high  $\sigma$ . In conclusion, the latent space, which is suitable for denoising tasks, contains not only noise level information but also global content information.

Moreover, we also present t-SNE visualization of the real-noise denoising in Fig. 8. We extract patches from three datasets: SIDD [40] validation set, DND [41], and DIV2K validation set [96] with synthetic noise following [38]. As shown in Fig. 8a, the latent embedding is highly correlated to the content information such as colors and intensities. It might be connected to the common knowledge that the noise from the real world is signal-dependent. Interestingly, based on Fig. 8b, the latent code captures different characteristics between the noise from SIDD [40] and DND [41], despite we did not inject any supervision about the dataset. Concretely, they are separately clustered, and we might infer that there exists a domain gap between them. In other words, our latent code sees the difference in the noise distribution of smartphone cameras and commercial cameras. Rather, the synthetic noise based on [38] better mimic the characteristics of the noise from DND compared to SIDD [40] based on our observation.

To verify this observation, we train a baseline network which is the restorer without the encoder-decoder network with two different training datasets: DIV2K [96] with synthetic noise [38], and SIDD [40]. The ablation results are presented in TABLE VIII. Interestingly, training with synthetic datasets shows poor results in SIDD, whereas the results on DND are quite moderate. In contrast, training with the SIDD training dataset shows decent results both in the SIDD validation set and DND. The overall observations are quite consistent with our latent embeddings, which are learned in an unsupervised manner. We may conclude that our latent representation provides informative cues relevant to the denoising objective.

### B. Ablation Study

We demonstrate ablation results on the loss terms in TABLE IX. Without the encoder-decoder, using only the restoration term  $\mathcal{L}_{res}$  corresponds to the naïve blind model, and the performance is inferior to other methods. Without the adversarial loss and the estimation loss, the reconstruction loss is a simple L1 loss. It shows a slightly inferior result compared to using full loss terms because the pixel-wise loss strictly assumes a probability distribution family. As the pixel-wise loss is known to generate blurry results, it tends to see more on structures, where the noise is more likely textures and details. Hence, the noise distribution cannot be well



Fig. 5: Latent space manipulation by feeding different input images to the encoder. For the denoiser, (a) we feed an input image with  $\sigma = 30$ . For the encoder, we feed four different inputs: (b) the same noisy image, (c) flipped noisy image, and (d-e) the same image with different noise levels.

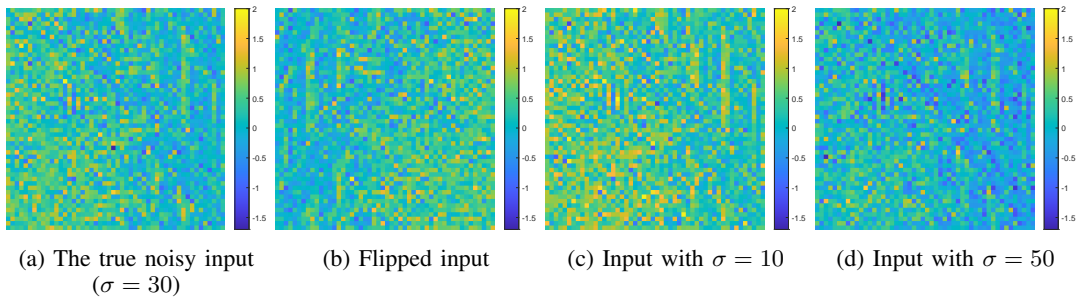


Fig. 6: Latent space visualization of Fig. 5. It can be seen that the latent variable reflects the noise level and image contents very well.

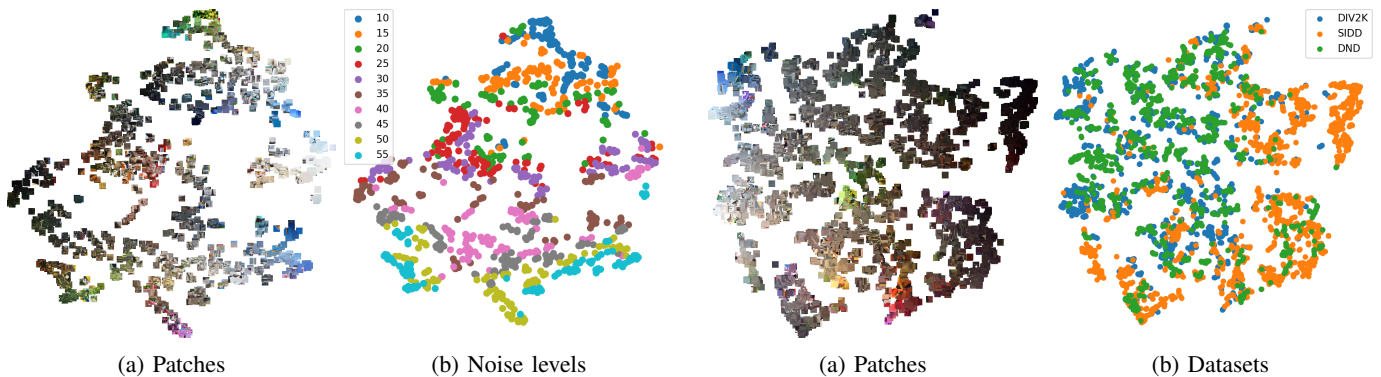


Fig. 7: t-SNE visualizations on Gaussian noise. (a) t-SNE visualization with patches. (b) Corresponding noise levels presented with different colors.

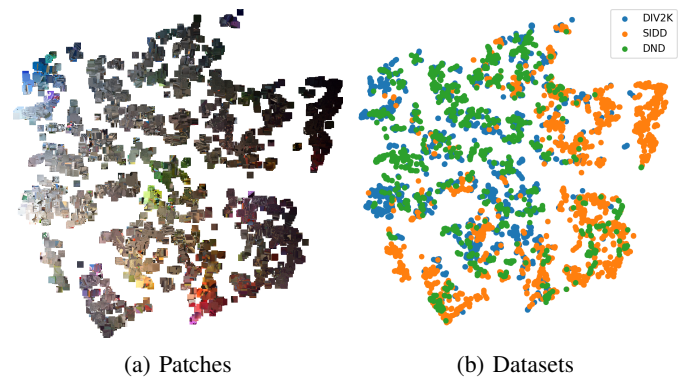


Fig. 8: t-SNE visualizations on real-noise. (a) t-SNE visualization with patches. (b) Corresponding datasets.

captured by pixel-wise loss terms. By using all loss terms, the proposed method guarantees the performance that surpasses the others. Consistent results on real-noise are presented in TABLE X. Note that the experiment is performed with the SIDD validation set in this case, instead of the test set that requires online submissions. In the case of DND, it is tested by submitting the results to the DND site because the validation set is not available.

For further investigation on the framework, we replace the denoiser with FFDNet [12] architecture and retrain with our

framework. The comparisons with the original FFDNet [12] are shown in TABLE XI. There exists noticeable performance gain due to our VDIR framework. From this result, we can see that the performance gain over FFDNet, shown in Tables I, II, and III, are not just from the use of more parameters. Specifically, we have the gains over the FFDNet by using the same-sized FFDNet architecture into our VDIR framework, which validates the effectiveness of our variational scheme. Also, it is noteworthy that the results of FFDNet are non-blind results, whereas our method is tested on blind conditions. Even though they are tested on different conditions, our framework

TABLE IX: Ablation study on CBSD68 with  $\sigma = 30$ .

Loss term	PSNR
$\mathcal{L}_{denoise}$	30.47
$\mathcal{L}_{denoise} + \beta D_{KL} + \mathcal{L}_{recon}$ w/o $\mathcal{L}_{adv}$	30.56
$\mathcal{L}_{denoise} + \beta D_{KL} + \mathcal{L}_{recon}$ w/ $\mathcal{L}_{adv}$	30.64

TABLE X: Ablation study on real-noise. ‘‘SIDD-val’’ means that the comparison is performed with the SIDD validation set.

Loss term	SIDD val	DND
$\mathcal{L}_{denoise}$	39.11	39.47
$\mathcal{L}_{full}$	39.29	39.63

boosts the performance. In conclusion, our framework does not only boost the performance, but also works as a noise level estimator, making the overall framework to be a blind denoiser, which is very effective.

## IX. CONCLUSION

We have proposed a novel universal variational approach for image restoration, which can be applied to many image restoration tasks. Concretely, we reformulated the joint distribution of the low-/high-quality images based on the proposed latent variable  $c$ , which brings out two inference problems. Then, we introduced a *variational lower bound* to approximate the inference problem of the latent variable. With our *variational lower bound*, the original inference problem can be simplified and divided into separate sub-problems. Our *variational lower bound* incorporates both the restoration objective and the reconstruction objective, which is a generative model on the low-quality image. Hence, the embedded information of complicated low-quality image manifold plays a role as additional prior information. We have also presented three parameterized CNNs for the inference problem and have shown that our method achieves state-of-the-art performance in several image restoration tasks while requiring moderate model capacity. Furthermore, we also presented more analyses of our framework in the *supplemental material* to demonstrate that our method has steerability, which can be applied to practical applications. Our code and some visualized results are available at <https://github.com/JWSoh/VDIR>.

## REFERENCES

- [1] L. I. Rudin, S. Osher, and E. Fatemi, ‘‘Nonlinear total variation based noise removal algorithms,’’ *Physica D: nonlinear phenomena*, vol. 60, no. 1–4, pp. 259–268, 1992.
- [2] M. Elad and M. Aharon, ‘‘Image denoising via sparse and redundant representations over learned dictionaries,’’ *IEEE Transactions on Image Processing*, vol. 15, no. 12, pp. 3736–3745, 2006.
- [3] A. Buades, B. Coll, and J.-M. Morel, ‘‘A non-local algorithm for image denoising,’’ in *2005 IEEE Computer Society Conference on Computer Vision and Pattern Recognition (CVPR’05)*, vol. 2. IEEE, 2005, pp. 60–65.
- [4] W. Dong, L. Zhang, G. Shi, and X. Li, ‘‘Nonlocally centralized sparse representation for image restoration,’’ *IEEE transactions on Image Processing*, vol. 22, no. 4, pp. 1620–1630, 2012.
- [5] J. Mairal, F. R. Bach, J. Ponce, G. Sapiro, and A. Zisserman, ‘‘Non-local sparse models for image restoration,’’ in *ICCV*, vol. 29. Citeseer, 2009, pp. 54–62.

TABLE XI: The results of the denoiser replaced by FFDNet [12] on Urban100.

Noise level	$\sigma = 30$	$\sigma = 50$
FFDNet [12]	30.53	28.05
Ours (FFDNet)	30.82	28.49
$\Delta$ PSNR	0.29	0.44

- [6] R. Timofte, V. De Smet, and L. Van Gool, ‘‘A+: Adjusted anchored neighborhood regression for fast super-resolution,’’ in *Asian conference on computer vision*. Springer, 2014, pp. 111–126.
- [7] S. Gu, L. Zhang, W. Zuo, and X. Feng, ‘‘Weighted nuclear norm minimization with application to image denoising,’’ in *Proceedings of the IEEE conference on computer vision and pattern recognition*, 2014, pp. 2862–2869.
- [8] K. Dabov, A. Foi, V. Katkovnik, and K. Egiazarian, ‘‘Image denoising by sparse 3-d transform-domain collaborative filtering,’’ *IEEE Transactions on image processing*, vol. 16, no. 8, pp. 2080–2095, 2007.
- [9] J. Xu, L. Zhang, and D. Zhang, ‘‘A trilateral weighted sparse coding scheme for real-world image denoising,’’ in *Proceedings of the European Conference on Computer Vision (ECCV)*, 2018, pp. 20–36.
- [10] P. Milanfar, ‘‘A tour of modern image filtering: New insights and methods, both practical and theoretical,’’ *IEEE signal processing magazine*, vol. 30, no. 1, pp. 106–128, 2012.
- [11] K. Zhang, W. Zuo, Y. Chen, D. Meng, and L. Zhang, ‘‘Beyond a gaussian denoiser: Residual learning of deep cnn for image denoising,’’ *IEEE Transactions on Image Processing*, vol. 26, no. 7, pp. 3142–3155, 2017.
- [12] K. Zhang, W. Zuo, and L. Zhang, ‘‘Ffdnet: Toward a fast and flexible solution for cnn-based image denoising,’’ *IEEE Transactions on Image Processing*, vol. 27, no. 9, pp. 4608–4622, 2018.
- [13] D. Liu, B. Wen, Y. Fan, C. C. Loy, and T. S. Huang, ‘‘Non-local recurrent network for image restoration,’’ in *Advances in Neural Information Processing Systems*, 2018, pp. 1673–1682.
- [14] Y. Zhang, K. Li, K. Li, B. Zhong, and Y. Fu, ‘‘Residual non-local attention networks for image restoration,’’ in *Proceedings of the International Conference on Learning Representation*, 2019.
- [15] C. Dong, C. C. Loy, K. He, and X. Tang, ‘‘Learning a deep convolutional network for image super-resolution,’’ in *European conference on computer vision*. Springer, 2014.
- [16] B. Lim, S. Son, H. Kim, S. Nah, and K. M. Lee, ‘‘Enhanced deep residual networks for single image super-resolution,’’ in *The IEEE conference on computer vision and pattern recognition (CVPR) workshops*, 2017.
- [17] J. Gu, H. Lu, W. Zuo, and C. Dong, ‘‘Blind super-resolution with iterative kernel correction,’’ in *Proceedings of the IEEE/CVF Conference on Computer Vision and Pattern Recognition*, 2019, pp. 1604–1613.
- [18] Y. Mei, Y. Fan, Y. Zhou, L. Huang, T. S. Huang, and H. Shi, ‘‘Image super-resolution with cross-scale non-local attention and exhaustive self-exemplars mining,’’ in *Proceedings of the IEEE/CVF Conference on Computer Vision and Pattern Recognition*, 2020, pp. 5690–5699.
- [19] C. Dong, Y. Deng, C. C. Loy, and X. Tang, ‘‘Compression artifacts reduction by a deep convolutional network,’’ in *Proceedings of the IEEE International Conference on Computer Vision*, 2015, pp. 576–584.
- [20] Y. Kim, J. W. Soh, and N. I. Cho, ‘‘Agarnet: adaptively gated jpeg compression artifacts removal network for a wide range quality factor,’’ *IEEE Access*, vol. 8, pp. 20 160–20 170, 2020.
- [21] K. Zhang, W. Zuo, and L. Zhang, ‘‘Learning a single convolutional super-resolution network for multiple degradations,’’ in *Proceedings of the IEEE Conference on Computer Vision and Pattern Recognition*, 2018, pp. 3262–3271.
- [22] A. Shocher, N. Cohen, and M. Irani, ‘‘Zero-shot super-resolution using deep internal learning,’’ in *Proceedings of the IEEE Conference on Computer Vision and Pattern Recognition*, 2018, pp. 3118–3126.
- [23] J. W. Soh, S. Cho, and N. I. Cho, ‘‘Meta-transfer learning for zero-shot super-resolution,’’ in *Proceedings of the IEEE/CVF Conference on Computer Vision and Pattern Recognition*, 2020, pp. 3516–3525.
- [24] K. Zhang, L. V. Gool, and R. Timofte, ‘‘Deep unfolding network for image super-resolution,’’ in *Proceedings of the IEEE/CVF Conference on Computer Vision and Pattern Recognition*, 2020, pp. 3217–3226.
- [25] Y.-S. Xu, S.-Y. R. Tseng, Y. Tseng, H.-K. Kuo, and Y.-M. Tsai, ‘‘Unified dynamic convolutional network for super-resolution with

- variational degradations,” in *Proceedings of the IEEE/CVF Conference on Computer Vision and Pattern Recognition*, 2020, pp. 12 496–12 505.
- [26] Y. Kim, J. W. Soh, and N. I. Cho, “Adaptively tuning a convolutional neural network by gate process for image denoising,” *IEEE Access*, vol. 7, pp. 63 447–63 456, 2019.
- [27] S. Bell-Kligler, A. Shocher, and M. Irani, “Blind super-resolution kernel estimation using an internal-gan,” in *Advances in neural information processing systems*, 2019.
- [28] Z. Yue, H. Yong, Q. Zhao, D. Meng, and L. Zhang, “Variational denoising network: Toward blind noise modeling and removal,” in *Advances in Neural Information Processing Systems*, 2019, pp. 1688–1699.
- [29] J. W. Soh and N. I. Cho, “Deep universal blind image denoising,” in *International Conference on Pattern Recognition*, 2020.
- [30] I. Goodfellow, J. Pouget-Abadie, M. Mirza, B. Xu, D. Warde-Farley, S. Ozair, A. Courville, and Y. Bengio, “Generative adversarial nets,” in *Advances in neural information processing systems*, 2014, pp. 2672–2680.
- [31] C. Ledig, L. Theis, F. Huszár, J. Caballero, A. Cunningham, A. Acosta, A. P. Aitken, A. Tejani, J. Totz, Z. Wang *et al.*, “Photo-realistic single image super-resolution using a generative adversarial network,” in *Proceedings of the IEEE conference on computer vision and pattern recognition*, 2017.
- [32] X. Wang, K. Yu, C. Dong, and C. C. Loy, “Recovering realistic texture in image super-resolution by deep spatial feature transform,” in *Proceedings of the IEEE conference on computer vision and pattern recognition*, 2018, pp. 606–615.
- [33] J. W. Soh, G. Y. Park, J. Jo, and N. I. Cho, “Natural and realistic single image super-resolution with explicit natural manifold discrimination,” in *The IEEE Conference on Computer Vision and Pattern Recognition (CVPR)*, June 2019.
- [34] W. Zhang, Y. Liu, C. Dong, and Y. Qiao, “Ranksrgan: Generative adversarial networks with ranker for image super-resolution,” in *Proceedings of the IEEE/CVF International Conference on Computer Vision*, 2019, pp. 3096–3105.
- [35] Y. Tai, J. Yang, X. Liu, and C. Xu, “Memnet: A persistent memory network for image restoration,” in *Proceedings of the IEEE international conference on computer vision*, 2017, pp. 4539–4547.
- [36] J. Kim, J. Kwon Lee, and K. Mu Lee, “Accurate image super-resolution using very deep convolutional networks,” in *Proceedings of the IEEE conference on computer vision and pattern recognition*, 2016, pp. 1646–1654.
- [37] S. Lefkimmiatis, “Universal denoising networks: a novel cnn architecture for image denoising,” in *Proceedings of the IEEE conference on computer vision and pattern recognition*, 2018, pp. 3204–3213.
- [38] S. Guo, Z. Yan, K. Zhang, W. Zuo, and L. Zhang, “Toward convolutional blind denoising of real photographs,” in *Proceedings of the IEEE Conference on Computer Vision and Pattern Recognition*, 2019, pp. 1712–1722.
- [39] S. Nam, Y. Hwang, Y. Matsushita, and S. Joo Kim, “A holistic approach to cross-channel image noise modeling and its application to image denoising,” in *Proceedings of the IEEE conference on computer vision and pattern recognition*, 2016, pp. 1683–1691.
- [40] A. Abdelhamed, S. Lin, and M. S. Brown, “A high-quality denoising dataset for smartphone cameras,” in *Proceedings of the IEEE Conference on Computer Vision and Pattern Recognition*, 2018, pp. 1692–1700.
- [41] T. Plotz and S. Roth, “Benchmarking denoising algorithms with real photographs,” in *The IEEE Conference on Computer Vision and Pattern Recognition (CVPR)*, July 2017.
- [42] S. Anwar and N. Barnes, “Real image denoising with feature attention,” in *Proceedings of the IEEE International Conference on Computer Vision*, 2019, pp. 3155–3164.
- [43] S. W. Zamir, A. Arora, S. Khan, M. Hayat, F. S. Khan, M.-H. Yang, and L. Shao, “Cycleisp: Real image restoration via improved data synthesis,” *arXiv preprint arXiv:2003.07761*, 2020.
- [44] C. Chen, Z. Xiong, X. Tian, Z.-J. Zha, and F. Wu, “Camera lens super-resolution,” in *Proceedings of the IEEE/CVF Conference on Computer Vision and Pattern Recognition*, 2019, pp. 1652–1660.
- [45] X. Zhang, Q. Chen, R. Ng, and V. Koltun, “Zoom to learn, learn to zoom,” in *Proceedings of the IEEE/CVF Conference on Computer Vision and Pattern Recognition*, 2019, pp. 3762–3770.
- [46] J. Cai, H. Zeng, H. Yong, Z. Cao, and L. Zhang, “Toward real-world single image super-resolution: A new benchmark and a new model,” in *Proceedings of the IEEE/CVF International Conference on Computer Vision*, 2019, pp. 3086–3095.
- [47] P. Wei, Z. Xie, H. Lu, Z. Zhan, Q. Ye, W. Zuo, and L. Lin, “Component divide-and-conquer for real-world image super-resolution,” in *European Conference on Computer Vision*. Springer, 2020, pp. 101–117.
- [48] A. Foi, M. Trimeche, V. Katkovnik, and K. Egiazarian, “Practical poissonian-gaussian noise modeling and fitting for single-image raw-data,” *IEEE Transactions on Image Processing*, vol. 17, no. 10, pp. 1737–1754, 2008.
- [49] A. Foi, “Clipped noisy images: Heteroskedastic modeling and practical denoising,” *Signal Processing*, vol. 89, no. 12, pp. 2609–2629, 2009.
- [50] M. Makitalo and A. Foi, “Optimal inversion of the generalized anscombe transformation for poisson-gaussian noise,” *IEEE transactions on image processing*, vol. 22, no. 1, pp. 91–103, 2012.
- [51] J. Zhang and K. Hirakawa, “Improved denoising via poisson mixture modeling of image sensor noise,” *IEEE Transactions on Image Processing*, vol. 26, no. 4, pp. 1565–1578, 2017.
- [52] T. Brooks, B. Mildenhall, T. Xue, J. Chen, D. Sharlet, and J. T. Barron, “Unprocessing images for learned raw denoising,” in *Proceedings of the IEEE Conference on Computer Vision and Pattern Recognition*, 2019, pp. 11 036–11 045.
- [53] K. Wei, Y. Fu, J. Yang, and H. Huang, “A physics-based noise formation model for extreme low-light raw denoising,” *arXiv preprint arXiv:2003.12751*, 2020.
- [54] X. Xu, Y. Ma, and W. Sun, “Towards real scene super-resolution with raw images,” in *Proceedings of the IEEE/CVF Conference on Computer Vision and Pattern Recognition*, 2019, pp. 1723–1731.
- [55] J. Chen, J. Chen, H. Chao, and M. Yang, “Image blind denoising with generative adversarial network based noise modeling,” in *Proceedings of the IEEE Conference on Computer Vision and Pattern Recognition*, 2018, pp. 3155–3164.
- [56] R. Zhou and S. Susstrunk, “Kernel modeling super-resolution on real low-resolution images,” in *Proceedings of the IEEE/CVF International Conference on Computer Vision*, 2019, pp. 2433–2443.
- [57] A. Abdelhamed, M. A. Brubaker, and M. S. Brown, “Noise flow: Noise modeling with conditional normalizing flows,” in *Proceedings of the IEEE International Conference on Computer Vision*, 2019, pp. 3165–3173.
- [58] Y. Zhang, K. Li, K. Li, L. Wang, B. Zhong, and Y. Fu, “Image super-resolution using very deep residual channel attention networks,” in *European Conference on Computer Vision*, 2018, pp. 286–301.
- [59] Z. Li, J. Yang, Z. Liu, X. Yang, G. Jeon, and W. Wu, “Feedback network for image super-resolution,” in *The IEEE Conference on Computer Vision and Pattern Recognition (CVPR)*, June 2019.
- [60] A. Gnansambandam and S. H. Chan, “One size fits all: Can we train one denoiser for all noise levels?” *Proceedings of the International Conference on Learning Representation*, 2020.
- [61] X. Hu, H. Mu, X. Zhang, Z. Wang, T. Tan, and J. Sun, “Meta-sr: a magnification-arbitrary network for super-resolution,” in *Proceedings of the IEEE Conference on Computer Vision and Pattern Recognition*, 2019, pp. 1575–1584.
- [62] Y. Kim, J. W. Soh, G. Y. Park, and N. I. Cho, “Transfer learning from synthetic to real-noise denoising with adaptive instance normalization,” in *Proceedings of the IEEE/CVF Conference on Computer Vision and Pattern Recognition*, 2020, pp. 3482–3492.
- [63] B. Ahn and N. I. Cho, “Block-matching convolutional neural network for image denoising,” *arXiv preprint arXiv:1704.00524*, 2017.
- [64] T. Guo, H. Seyed Mousavi, T. Huu Vu, and V. Monga, “Deep wavelet prediction for image super-resolution,” in *Proceedings of the IEEE Conference on Computer Vision and Pattern Recognition Workshops*, 2017, pp. 104–113.
- [65] P. Liu, H. Zhang, K. Zhang, L. Lin, and W. Zuo, “Multi-level wavelet-cnn for image restoration,” in *Proceedings of the IEEE conference on computer vision and pattern recognition workshops*, 2018, pp. 773–782.
- [66] H. Huang, R. He, Z. Sun, and T. Tan, “Wavelet-srnet: A wavelet-based cnn for multi-scale face super resolution,” in *Proceedings of the IEEE International Conference on Computer Vision*, 2017, pp. 1689–1697.
- [67] A. Bulat and G. Tzimiropoulos, “Super-fan: Integrated facial landmark localization and super-resolution of real-world low resolution faces in arbitrary poses with gans,” in *Proceedings of the IEEE Conference on Computer Vision and Pattern Recognition*, 2018, pp. 109–117.
- [68] Y. Chen, Y. Tai, X. Liu, C. Shen, and J. Yang, “Fsrnet: End-to-end learning face super-resolution with facial priors,” in *Proceedings of the IEEE Conference on Computer Vision and Pattern Recognition*, 2018, pp. 2492–2501.

- [69] J. W. Soh, J. Park, Y. Kim, B. Ahn, H.-S. Lee, Y.-S. Moon, and N. I. Cho, "Reduction of video compression artifacts based on deep temporal networks," *IEEE Access*, vol. 6, pp. 63 094–63 106, 2018.
- [70] A. Kappeler, S. Yoo, Q. Dai, and A. K. Katsaggelos, "Video super-resolution with convolutional neural networks," *IEEE Transactions on Computational Imaging*, vol. 2, no. 2, pp. 109–122, 2016.
- [71] M. S. Sajjadi, R. Vemulapalli, and M. Brown, "Frame-recurrent video super-resolution," in *Proceedings of the IEEE Conference on Computer Vision and Pattern Recognition*, 2018, pp. 6626–6634.
- [72] T. Xue, B. Chen, J. Wu, D. Wei, and W. T. Freeman, "Video enhancement with task-oriented flow," *International Journal of Computer Vision*, vol. 127, no. 8, pp. 1106–1125, 2019.
- [73] Y. Tian, Y. Zhang, Y. Fu, and C. Xu, "Tdan: Temporally-deformable alignment network for video super-resolution," in *Proceedings of the IEEE/CVF Conference on Computer Vision and Pattern Recognition*, 2020, pp. 3360–3369.
- [74] X. Liu, M. Suganuma, Z. Sun, and T. Okatani, "Dual residual networks leveraging the potential of paired operations for image restoration," in *Proceedings of the IEEE/CVF Conference on Computer Vision and Pattern Recognition*, 2019, pp. 7007–7016.
- [75] T. Karras, S. Laine, and T. Aila, "A style-based generator architecture for generative adversarial networks," in *Proceedings of the IEEE/CVF Conference on Computer Vision and Pattern Recognition*, 2019, pp. 4401–4410.
- [76] T. Karras, S. Laine, M. Aittala, J. Hellsten, J. Lehtinen, and T. Aila, "Analyzing and improving the image quality of stylegan," in *Proceedings of the IEEE/CVF Conference on Computer Vision and Pattern Recognition*, 2020, pp. 8110–8119.
- [77] J. Gu, Y. Shen, and B. Zhou, "Image processing using multi-code gan prior," in *Proceedings of the IEEE/CVF conference on computer vision and pattern recognition*, 2020, pp. 3012–3021.
- [78] K. C. Chan, X. Wang, X. Xu, J. Gu, and C. C. Loy, "Glean: Generative latent bank for large-factor image super-resolution," in *Proceedings of the IEEE/CVF Conference on Computer Vision and Pattern Recognition*, 2021, pp. 14 245–14 254.
- [79] X. Pan, X. Zhan, B. Dai, D. Lin, C. C. Loy, and P. Luo, "Exploiting deep generative prior for versatile image restoration and manipulation," *IEEE Transactions on Pattern Analysis and Machine Intelligence*, 2021.
- [80] Z. Chi, Y. Wang, Y. Yu, and J. Tang, "Test-time fast adaptation for dynamic scene deblurring via meta-auxiliary learning," in *Proceedings of the IEEE/CVF Conference on Computer Vision and Pattern Recognition*, 2021, pp. 9137–9146.
- [81] D. Ritchie, P. Horsfall, and N. D. Goodman, "Deep amortized inference for probabilistic programs," *arXiv preprint arXiv:1610.05735*, 2016.
- [82] C. Zhang, J. Bütepage, H. Kjellström, and S. Mandt, "Advances in variational inference," *IEEE transactions on pattern analysis and machine intelligence*, vol. 41, no. 8, pp. 2008–2026, 2018.
- [83] D. P. Kingma and M. Welling, "Auto-encoding variational bayes," *Proceedings of the International Conference on Learning Representation*, 2014.
- [84] I. Higgins, L. Matthey, A. Pal, C. Burgess, X. Glorot, M. Botvinick, S. Mohamed, and A. Lerchner, "beta-vae: Learning basic visual concepts with a constrained variational framework," *Proceedings of the International Conference on Learning Representation*, vol. 2, no. 5, p. 6, 2017.
- [85] D. Ren, W. Zuo, D. Zhang, L. Zhang, and M.-H. Yang, "Simultaneous fidelity and regularization learning for image restoration," *IEEE transactions on pattern analysis and machine intelligence*, vol. 43, no. 1, pp. 284–299, 2019.
- [86] K. Zhang, W. Zuo, and L. Zhang, "Deep plug-and-play super-resolution for arbitrary blur kernels," in *Proceedings of the IEEE/CVF Conference on Computer Vision and Pattern Recognition*, 2019, pp. 1671–1681.
- [87] R. Liu, P. Mu, J. Chen, X. Fan, and Z. Luo, "Investigating task-driven latent feasibility for nonconvex image modeling," *IEEE Transactions on Image Processing*, vol. 29, pp. 7629–7640, 2020.
- [88] K. Zhang, Y. Li, W. Zuo, L. Zhang, L. Van Gool, and R. Timofte, "Plug-and-play image restoration with deep denoiser prior," *IEEE Transactions on Pattern Analysis and Machine Intelligence*, 2021.
- [89] K. He, X. Zhang, S. Ren, and J. Sun, "Deep residual learning for image recognition," in *Proceedings of the IEEE conference on computer vision and pattern recognition*, 2016, pp. 770–778.
- [90] W. Shi, J. Caballero, F. Huszár, J. Totz, A. P. Aitken, R. Bishop, D. Rueckert, and Z. Wang, "Real-time single image and video super-resolution using an efficient sub-pixel convolutional neural network," in *Proceedings of the IEEE conference on computer vision and pattern recognition*, 2016, pp. 1874–1883.
- [91] Y. Chen and T. Pock, "Trainable nonlinear reaction diffusion: A flexible framework for fast and effective image restoration," *IEEE transactions on pattern analysis and machine intelligence*, vol. 39, no. 6, pp. 1256–1272, 2016.
- [92] S. W. Zamir, A. Arora, S. Khan, M. Hayat, F. S. Khan, M.-H. Yang, and L. Shao, "Learning enriched features for real image restoration and enhancement," in *Computer Vision—ECCV 2020: 16th European Conference, Glasgow, UK, August 23–28, 2020, Proceedings, Part XXV 16*. Springer, 2020, pp. 492–511.
- [93] —, "Multi-stage progressive image restoration," in *Proceedings of the IEEE/CVF Conference on Computer Vision and Pattern Recognition*, 2021, pp. 14 821–14 831.
- [94] Y. Liu, Z. Qin, S. Anwar, P. Ji, D. Kim, S. Caldwell, and T. Gedeon, "Invertible denoising network: A light solution for real noise removal," in *Proceedings of the IEEE/CVF Conference on Computer Vision and Pattern Recognition*, 2021, pp. 13 365–13 374.
- [95] J. Liang, K. Zhang, S. Gu, L. Van Gool, and R. Timofte, "Flow-based kernel prior with application to blind super-resolution," in *Proceedings of the IEEE/CVF Conference on Computer Vision and Pattern Recognition*, 2021, pp. 10 601–10 610.
- [96] E. Agustsson and R. Timofte, "Ntire 2017 challenge on single image super-resolution: Dataset and study," in *Proceedings of the IEEE Conference on Computer Vision and Pattern Recognition Workshops*, 2017, pp. 126–135.
- [97] D. Martin, C. Fowlkes, D. Tal, and J. Malik, "A database of human segmented natural images and its application to evaluating segmentation algorithms and measuring ecological statistics," in *Proceedings Eighth IEEE International Conference on Computer Vision. ICCV 2001*, vol. 2. IEEE, 2001, pp. 416–423.
- [98] J.-B. Huang, A. Singh, and N. Ahuja, "Single image super-resolution from transformed self-exemplars," in *Proceedings of the IEEE conference on computer vision and pattern recognition*, 2015, pp. 5197–5206.
- [99] Z. Wang, A. C. Bovik, H. R. Sheikh, and E. P. Simoncelli, "Image quality assessment: from error visibility to structural similarity," *IEEE transactions on image processing*, vol. 13, no. 4, pp. 600–612, 2004.
- [100] R. Timofte, R. Rothe, and L. Van Gool, "Seven ways to improve example-based single image super resolution," in *Proceedings of the IEEE Conference on Computer Vision and Pattern Recognition*, 2016, pp. 1865–1873.
- [101] J. Guo and H. Chao, "One-to-many network for visually pleasing compression artifacts reduction," in *Proceedings of the IEEE Conference on Computer Vision and Pattern Recognition*, 2017, pp. 3038–3047.
- [102] L. Galteri, L. Seidenari, M. Bertini, and A. Del Bimbo, "Deep generative adversarial compression artifact removal," in *Proceedings of the IEEE International Conference on Computer Vision*, 2017, pp. 4826–4835.
- [103] H. R. Sheikh, M. F. Sabir, and A. C. Bovik, "A statistical evaluation of recent full reference image quality assessment algorithms," *IEEE Transactions on image processing*, vol. 15, no. 11, pp. 3440–3451, 2006.
- [104] W. B. Pennebaker and J. L. Mitchell, *JPEG: Still image data compression standard*. Springer Science & Business Media, 1992.
- [105] L. v. d. Maaten and G. Hinton, "Visualizing data using t-sne," *Journal of machine learning research*, vol. 9, no. Nov, pp. 2579–2605, 2008.